Journal of Non-Newtonian Fluid Mechanics 227 (2016) 65–79

Contents lists available at ScienceDirect

Journal of Non-Newtonian Fluid Mechanics

journal homepage: www.elsevier.com/locate/jnnfm

Influence of channel aspect ratio on the onset of purely-elastic flow instabilities in three-dimensional planar cross-slots

F.A. Cruz [a], R.J. Poole [b], A.M. Afonso [a], F.T. Pinho [c], P.J. Oliveira [d], M.A. Alves [a,*]

[a] CEFT, Departamento de Engenharia Química, Faculdade de Engenharia da Universidade do Porto, Rua Dr. Roberto Frias, 4200-465 Porto, Portugal
[b] School of Engineering, University of Liverpool, Brownlow Street, Liverpool L69 3GH United Kingdom
[c] CEFT, Departamento de Engenharia Mecânica, Faculdade de Engenharia, Universidade do Porto, Rua Dr. Roberto Frias, 4200-465 Porto, Portugal
[d] Departamento de Engenharia Electromecânica, C-MAST, Universidade da Beira Interior, 6201-001 Covilhã, Portugal

ARTICLE INFO

Article history:
Received 15 August 2015
Revised 11 November 2015
Accepted 19 November 2015
Available online 2 December 2015

Keywords:
Finite-volume method
Cross-slot flow
Elastic instability
Stagnation-point flow
Steady flow bifurcation
Modified Pakdel–McKinley criterion

ABSTRACT

In this work, we perform creeping-flow simulations of upper-convected Maxwell and simplified Phan-Thien–Tanner fluids to study the purely-elastic steady bifurcation and transition to time-dependent flow in three-dimensional planar cross-slots. By analysing the flow in geometries with aspect ratios ranging from the near Hele-Shaw flow like limit, up to the very deep, two-dimensional limit, we are able to characterize the mechanism of the cross-slot bifurcation with significant detail. We conclude that the bifurcation mechanism is similar to a buckling instability, by which fluid is redirected *via* paths of least resistance, resulting in the emergence of peripheral stagnation points, above and below the central stagnation point. The intake of matter at the centre *via* the inlet axis is thus reduced, being compensated by fluid flowing through low resistance corridors along the central vertical axis, above and below the central point. Furthermore, we propose and locally compute a modified Pakdel–McKinley criterion, thereby producing a scalar stability field and suggesting emergent peripheral stagnation points also indirectly contribute to the onset of time-dependent flow.

1. Introduction

Elastic instabilities have been known to occur in several viscoelastic flows, such as Taylor–Couette flow and flow in extrusion devices, to name a few (see [1,2] for historical context). These instabilities, which may occur at vanishingly low Reynolds number (*Re*) flows, in which case the designation *purely-elastic* applies, may either be periodic time-dependent, as in the examples listed above, chaotic as observed in so-called elastic turbulence [3,4], or stationary, namely the asymmetric steady flow patterns observed in cross-slot geometries [5,6]. The steady asymmetries observed in two-dimensional cross-slots are known to result from a bifurcation, and lead to decreased flow resistance and thus a reduction in dissipated energy [7,8]. Depending on fluid rheology, the two-dimensional flow may also transition from a steady symmetric to a time-dependent state [9]. Although the steady flow bifurcation has been extensively studied from a two-dimensional (2D) perspective and results show energy dissipation decrease in the form of a reduced pressure drop, a mechanistic understanding of the phenomenon may benefit from an exploration of the three-dimensional (3D) nature of the flow bifurcation. Although there is a computational study which considers a 3D six-arm variant of the standard cross-slot [10], the mechanism of the bifurcation phenomenon is not explored in depth and the geometry *per se* is inherently not the same as the conventional four-arm planar cross-slot typically used in microfluidic devices. Furthermore, to the best of our knowledge, no other studies have attempted to characterize the 3D nature of the cross-slot bifurcation. However, stationary viscoelastic creeping-flow bifurcations are not unique to cross-slot geometries, and have been studied experimentally [11,12] and computationally [13] for flow past a confined cylinder, in flow-focusing devices [14], in T-shaped microchannels [15] and in mixing-separating cells [16]. Notably, the three-dimensional nature of the phenomenon in the flow past a confined cylinder has been explored in detail, and experimental studies report the formation of steady 3D flow cells in the cylinder wake upon bifurcation [11–13], with subsequent transition to time-dependent flow for increasing Deborah number (*De*), as also observed for cross-slot geometries [5-8]. The cellular structure found in the cylinder wake is characterized by spanwise, spatial-periodic asymmetries relative to the neutral axis of the wake and the convergence of streamlines into bundles, also arranged in a spatial-periodic manner (*cf.* Fig. 4 in Ref. [13]). This would indicate the fluid, upon steady bifurcation, selects a set of optimal flow paths, an idea consistent with the lower

* Corresponding author. Tel. +351 225081680; fax: +351 22 5081449.
E-mail address: mmalves@fe.up.pt (M.A. Alves).

http://dx.doi.org/10.1016/j.jnnfm.2015.11.008

energy dissipation observed in bifurcated 2D cross-slot creeping-flow, and which may hint at the mechanism of bifurcation in 3D cross-slots. Furthermore, McKinley et al. [11] have shown that the critical bifurcation *De* decreases as the cylinder blockage ratio increases, an observation suggesting an aspect ratio (*AR*) – defined as height/width – dependence of critical conditions for 3D cross-slots. Here, the cylinder blockage ratio and the cross-slot aspect ratio are compared on the basis that the fluid is forced through a narrower gap for higher cylinder blockage ratios or lower cross-slot aspect ratios, therefore producing increased shear-rates. In fact, earlier computational work [17] has lead us to anticipate a possible linear relation between the critical *De* and aspect ratio (*AR*), for $AR < 1$, implicitly invoking the Pakdel–McKinley criterion [18,19] due to the progressively larger tensile stress and velocity gradient near the cross-slot corners as the channel depth decreases. It should be noted however that for $AR < 1$, usually the flow field transitions directly from a steady symmetric to a time-dependent state, omitting the intermediate, stationary asymmetric configuration. Incidentally, it was also previously shown, for electro-osmotic viscoelastic flows in 2D cross-slots, that the stability of flow can be explained by a simplified model of flow around corners and application of the Pakdel–McKinley criterion therein [20].

In this work, we systematically study numerically the three-dimensional nature of the cross-slot steady flow bifurcation and also attempt to provide insights into the steady-unsteady transition. Using upper-convected Maxwell (UCM) [21] and Phan-Thien–Tanner (PTT) [22] constitutive equations, under creeping-flow conditions ($Re \to 0$), we simulate flow in planar, four-arm cross-slots, with aspect ratios ranging from close to the shallow, Hele-Shaw flow limit [23] up to very deep channels.

2. Numerical methods

We assume inertialess ($Re \to 0$), isothermal and incompressible three-dimensional flow. The governing equations are the continuity equation,

$$\nabla \cdot \mathbf{u} = 0, \tag{1}$$

the momentum equation,

$$-\nabla p + \nabla \cdot \boldsymbol{\tau} + \eta_s \nabla^2 \mathbf{u} = 0, \tag{2}$$

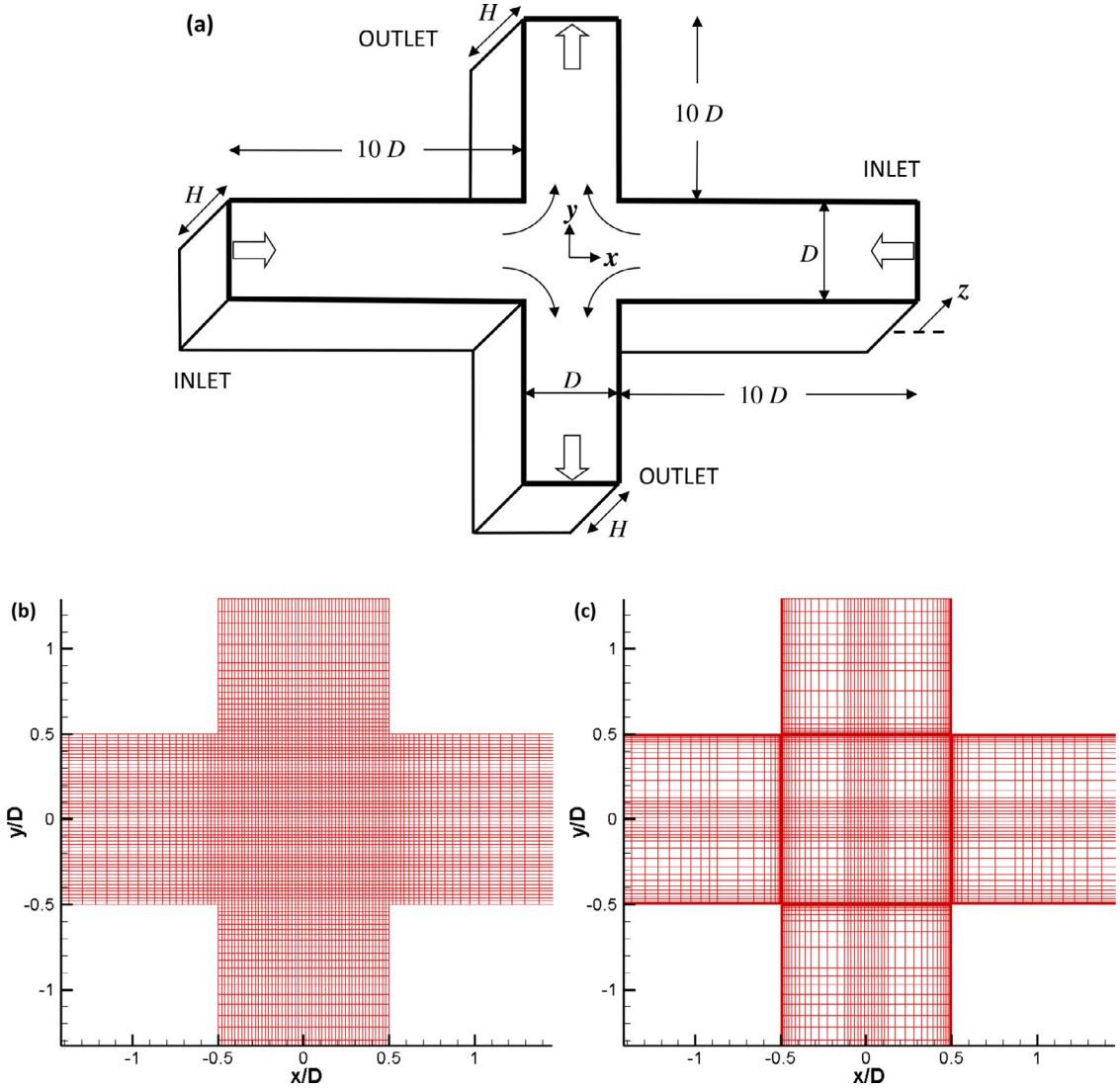

Fig. 1. (a) Schematic of the three-dimensional planar cross-slot geometry. (b, c) Zoomed-in, bird's eye view of the computational meshes. Mesh (b) is used for aspect ratios ranging from $ARn = 0.2$ to $ARn = 1.0$. Mesh (c) is used for $ARn = 0.01$ and $ARn = 0.1$; note the local refinement near the corners and lateral walls, obtained at the expense of a local coarsening away from the walls; care was taken to preserve cell density along the centrelines of the *x*- and *y*-axes. Cells in the four arms are progressively larger in the streamwise direction towards the inlets and outlets.

and a constitutive equation needed for the computation of the polymeric extra stress-tensor τ,

$$\left(1+\frac{\lambda_0\varepsilon}{\eta_{p,0}}\mathrm{Tr}(\boldsymbol{\tau})\right)\boldsymbol{\tau}+\lambda_0\left[\frac{\partial\boldsymbol{\tau}}{\partial t}+\nabla\cdot\mathbf{u}\boldsymbol{\tau}\right] = \eta_{p,0}\left(\nabla\mathbf{u}+\nabla\mathbf{u}^{\dagger}\right)+\lambda_0\left(\boldsymbol{\tau}\cdot\nabla\mathbf{u}+\nabla\mathbf{u}^{\dagger}\cdot\boldsymbol{\tau}\right), \quad (3)$$

representative of the simplified Phan-Thien–Tanner model with linear stress function, henceforth denoted sPTT [22,24], where λ_0 is the zero-shear-rate polymeric relaxation time, $\eta_{p,0}$ is the zero-shear-rate polymer viscosity, η_s is the solvent viscosity and ε is the extensibility parameter. Should the extensibility parameter ε be equal to zero, *i.e.* polymer chains with unlimited extensibilities, the constitutive model simplifies to an Oldroyd-B fluid [21], which is further simplified to the UCM model for solvent viscosity η_s equal to zero. Only two constitutive models are investigated in this work, the UCM fluid and the sPTT fluid with $\varepsilon = 0.02$ and $\beta = 1/9$, where β is the solvent viscosity ratio, defined as $\beta = \eta_s/(\eta_s+\eta_{p,0}) = \eta_s/\eta_0$, with η_0 being the zero-shear-rate solution viscosity. We note here the shear-thinning behaviour of the sPTT formulation, expressed by $\lambda_{eff} = \lambda_0/g(\boldsymbol{\tau})$ and $\eta_{p,eff} = \eta_{p,0}/g(\boldsymbol{\tau})$, with the subscript *eff* denoting effective values and the function $g(\boldsymbol{\tau})$ given by

$$g(\boldsymbol{\tau}) = 1+\frac{\lambda_0\varepsilon}{\eta_{p,0}}\mathrm{Tr}(\boldsymbol{\tau}). \quad (4)$$

An implicit, second-order, finite volume numerical method is used to solve the governing equations, as extensively described elsewhere [25–27], and to improve numerical stability the log-conformation technique [28] is applied. For each constitutive model-geometry pair, simulations were performed at progressively higher Deborah numbers, $De = \lambda_0 U/D$, where U is the average velocity in the four arms and D is the channel width, until unsteady flow conditions are attained. Viscometric flow is assumed near the walls, fully-developed velocity and stress profiles are given at the inlets and Neumann boundary conditions are assumed at the outlets for all variables, except pressure which is linearly extrapolated from the two

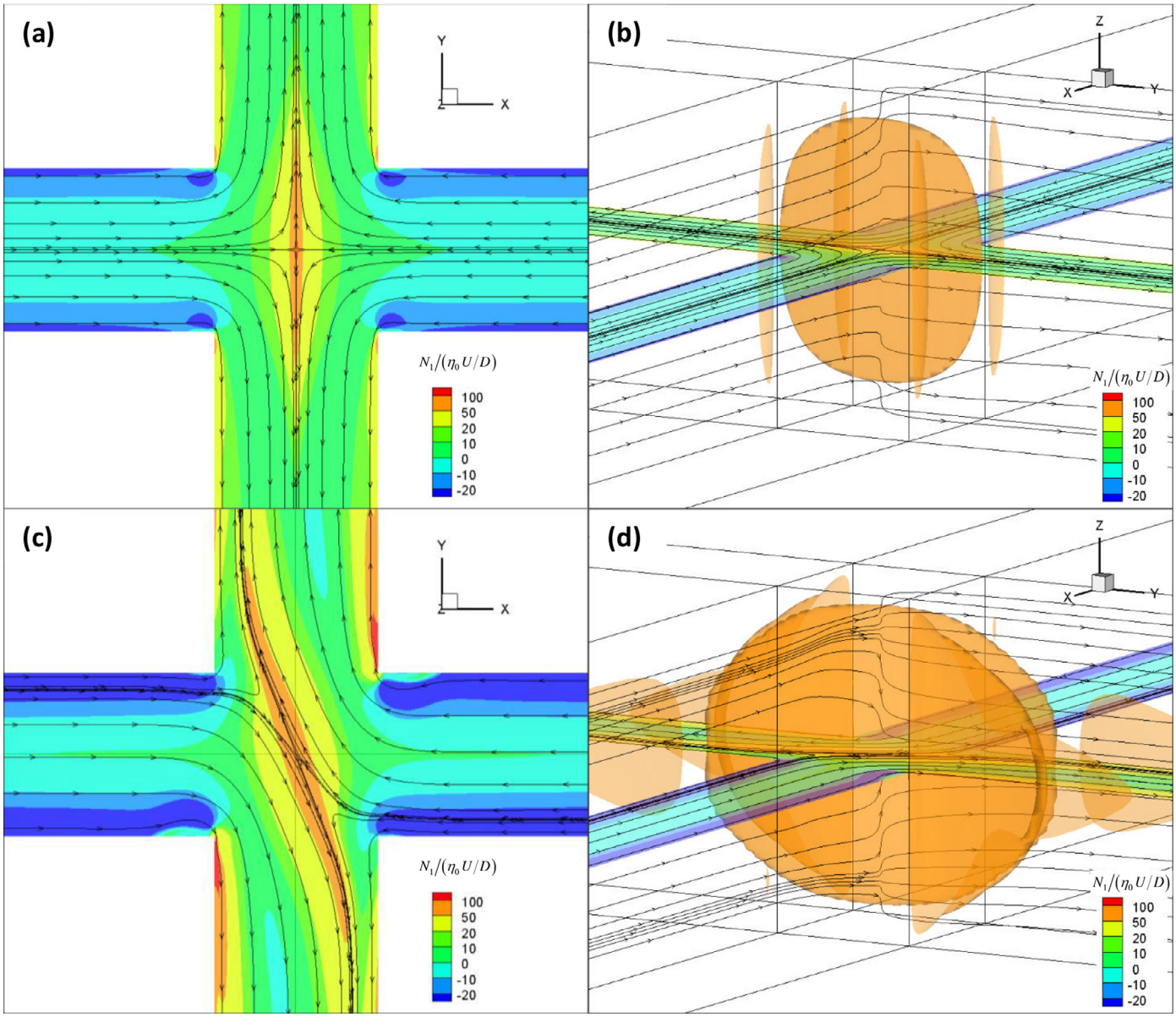

Fig. 2. Example of creeping-flow of the UCM fluid in a cross-slot channel with normalized aspect ratio $ARn = 0.7$. The flow is (a, b) steady symmetric at $De = 0.2$ and (c, d) steady asymmetric at $De = 0.4$. Panels (a, c) show the *XY* centre plane, at $z = 0$, with streamlines superimposed onto contour plots of the first normal stress difference, $N_1 = \tau_{yy} - \tau_{xx}$. Panels (b, d) show the corresponding three-dimensional iso-surface at $N_1/(\eta_0 U/D) = 50$ and streamlines originating on the $y = 0$ plane inside the inlet channel and crossing the central z-axis at various heights. The streamlines in panels (a, c) do not leave the centre plane.

upstream cells. No finite disturbances are introduced in the simulations to induce the onset of flow asymmetries or other instabilities. Instead, these solutions develop naturally from accumulation of round-off error at machine level precision – double precision FORTRAN is used for all calculations. A total of eleven meshes are used, all with the basic geometry given in Fig. 1(a). Each mesh has a different aspect ratio AR, defined as the ratio of height-to-width, $AR = H/D$, and is composed of five blocks, one for each arm and a fifth block for the central slot, each with 51^3 control volumes, totalling 663,255 computational cells. All meshes have the same total number of cells. To facilitate the representation of the widest possible range of aspect ratios, a normalized aspect ratio ARn is defined,

$$ARn = \frac{AR}{AR+1} = \frac{H}{H+D}. \tag{5}$$

The limits $ARn \to 0$ and $ARn \to 1$ correspond to the shallow and deep cross-slots, respectively. The former is the Hele-Shaw flow limit, while the latter is nominally equivalent to a 2D geometry. We distinguish truly 2D simulations as $ARn = 1.0$ and 3D simulations in deep channels as $ARn \to 1$. The exact range of aspect ratios covered is given in Table 1 along with other mesh characteristics. For the shallowest geometries, $ARn = 0.01$ and $ARn = 0.1$, acceptable resolution of velocity gradients near the cross-slot corners requires localized mesh refinement (Fig. 1(c)).

To facilitate the assessment of several important flow parameters, we compute the eigenvalues and eigenvectors of the tensor $(\nabla \mathbf{u}^\dagger)_{ij} = \partial u_i / \partial x_j$ at the stagnation point located at the geometric centre of the cross-slot. Assuming a linear velocity field in the vicinity of the central stagnation point, $\mathbf{u} = \nabla \mathbf{u}^\dagger \cdot \mathbf{x}$, the unit eigenvectors $\hat{\mathbf{v}}_n$ and eigenvalues ξ_n of $\nabla \mathbf{u}^\dagger$ represent the directions of the stagnation streamlines and the corresponding velocity gradients in streamline coordinates $\mathrm{d}\|\mathbf{u}\|/\mathrm{d}s_n$.

For incompressible creeping Newtonian flow, the three eigenvectors are the Cartesian unit vectors $(\hat{\mathbf{i}}, \hat{\mathbf{j}}, \hat{\mathbf{k}})$ and the corresponding

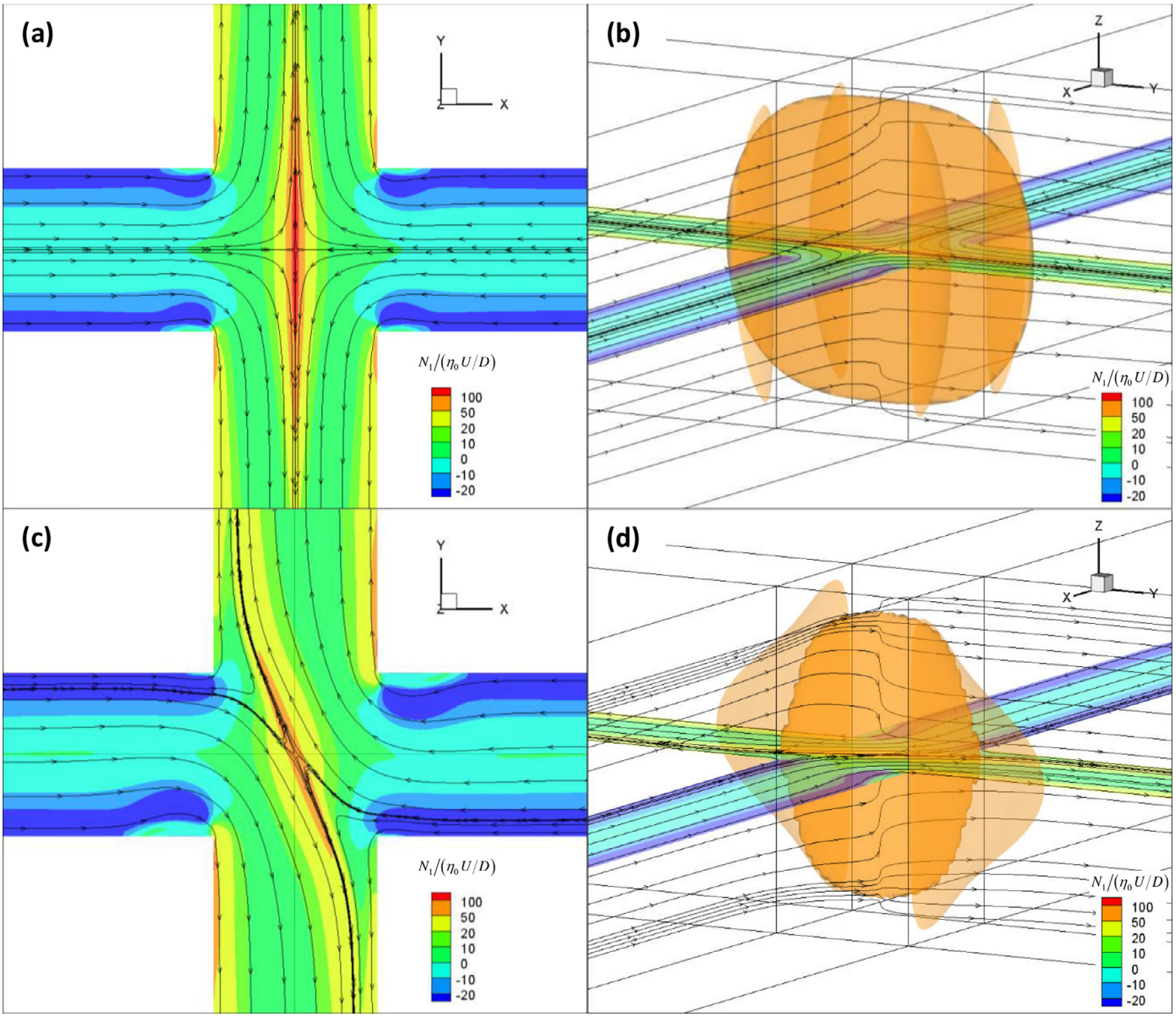

Fig. 3. Example of creeping-flow of the sPTT fluid with $\varepsilon = 0.02$ and $\beta = 1/9$ in a cross-slot channel with normalized aspect ratio $ARn = 0.7$. Flow is (a, b) steady symmetric at $De = 0.5$ and (c, d) steady asymmetric at $De = 1.1$. Panels (a, c) show the XY centre plane, at $z = 0$, with streamlines superimposed onto contour plots of the polymeric first normal stress difference, $N_1 = \tau_{yy} - \tau_{xx}$. Panels (b, d) show the corresponding three-dimensional iso-surface at $N_1/(\eta_0 U/D) = 50$ and streamlines originating on the $y = 0$ plane inside the inlet channel and crossing the central z-axis at various heights. The streamlines in panels (a, c) do not leave the centre plane.

Table 1
Characteristics of the computational meshes. All meshes are composed of five blocks, each with 51^3 cells, for a total of 663,255 cells. Cells along the z-direction are uniformly spaced, see Fig. 1 for cell spacing along the x- and y-directions.

ARn	*AR*	$\Delta z/D$
0.01	0.010	0.00020
0.1	0.11	0.0022
0.2	0.25	0.0049
0.3	0.43	0.0084
0.4	0.67	0.013
0.5	1.0	0.020
0.6	1.5	0.029
0.7	2.3	0.046
0.8	4.0	0.078
0.9	9.0	0.18
1.0	$\rightarrow \infty$	2D

strain-rates are $(-\dot{\varepsilon}_{stretch}, \dot{\varepsilon}_{stretch}, 0)$ for inlets along the x-direction and outlets along the y-direction, as sketched in Fig. 1. Furthermore, the continuity equation dictates that the sum of the three eigenvalues is equal to zero, regardless of flow configuration, and thus it is possible that up to two of the strain-rates are either positive or negative, implying the potential for stretching in more than one direction. We use the second eigenvalue ξ_2, along outlet direction $\hat{\mathbf{j}}$ for Newtonian flow or symmetric viscoelastic flow, as the magnitude of the extension-rate $\dot{\varepsilon}_{stretch}$. In the following, we refer to $\hat{\mathbf{k}}$ along the z-axis as the vertical direction, with the 3D cross-slot orientated in the XY centre plane as shown in Fig. 1. We note that the coordinate system defined by the eigenvectors $(\hat{\mathbf{v}}_1, \hat{\mathbf{v}}_2, \hat{\mathbf{v}}_3)$ of $\nabla \mathbf{u}^{\dagger}$ can be distinct from the standard Cartesian unit vectors $(\hat{\mathbf{i}}, \hat{\mathbf{j}}, \hat{\mathbf{k}})$, specifically if the flow field is asymmetric at the central stagnation point. It should be noted, however, that at the central stagnation point $\hat{\mathbf{k}} \equiv \hat{\mathbf{v}}_3$ across our data range.

3. Numerical results and discussion

3.1. Qualitative analysis of results and stability maps

Figs. 2 and 3 illustrate typical results for both UCM and sPTT models, respectively, presented for the same normalized aspect ratio ($ARn = 0.7$) to facilitate comparison. Represented are streamlines along the XY centre plane ($z = 0$) and crossing the central vertical axis at various heights, as well as the polymeric component of the first normal stress difference, $N_1 = \tau_{yy} - \tau_{xx}$, in dimensionless form. The highest De flows for this aspect ratio are represented, both prior to the steady bifurcation – (a) and (b) in both figures – and to the onset of time-dependent flow – (c) and (d).

Several observations may be drawn from Figs. 2 and 3, which are qualitatively similar, so the following applies to both. In panel (a), the predominantly extensional nature of the flow is noticeable along the outlet axis ($\hat{\mathbf{v}}_2$ direction). Accordingly, in panel (b) there is a well-defined region of large N_1, with the approximate shape of an ellipsoid, aligned with the YZ centre plane. Furthermore,

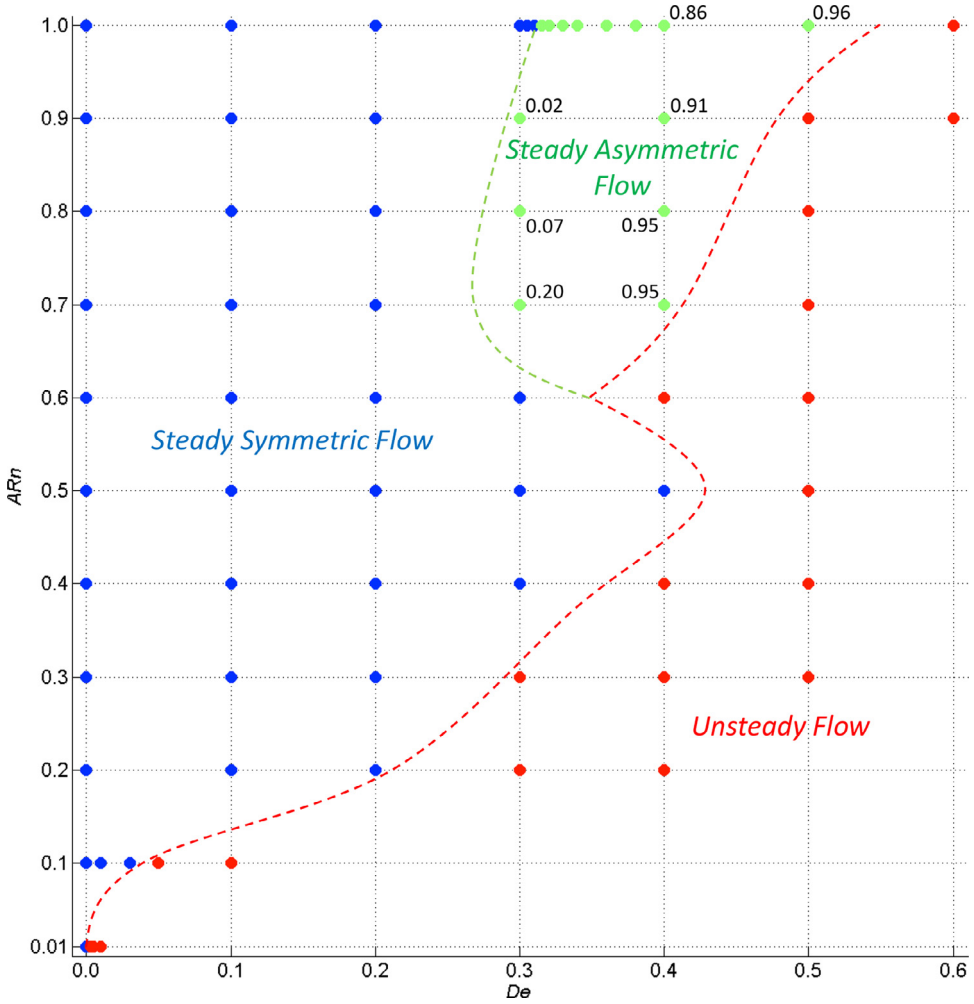

Fig. 4. Stability diagram for UCM fluid. Values are given for the cosine of the angle between non-vertical eigenvectors $(\hat{\mathbf{v}}_1, \hat{\mathbf{v}}_2)$ of $\nabla \mathbf{u}^{\dagger}$ at the centre of the cross-slot. The dashed lines are a guide to the eye.

streamlines drawn along the vertical central axis show a redirection of matter away from the stagnation point ($\xi_3 > 0$), as expected in a vertical stretch scenario. Regions of large normal stresses are also seen around the corners in panel (b). In a bifurcated state, the flow structure changes significantly. From the streamline distribution along the vertical axis in panel (d), two additional stagnation points are visible, one in the upper half ($z > 0$) and the other in the lower half ($z < 0$) of the slot. In-between these peripheral stagnation points and the centre of the channel, along the vertical z-direction, streamlines appear to show a redirection of matter towards the centre, which, by continuity, implies flow along the XY centre plane will have a tendency to avoid the principal stagnation point. Interestingly, despite the asymmetries along the horizontal middle-plane, vertical symmetry is seen relative to $z = 0$. Furthermore, large regions of high N_1 are seen in panel (d). The above mentioned birefringence ellipsoid strand has rotated around the z-axis to be aligned with the asymmetric flow pattern, and regions of high normal stresses around the corners have expanded significantly, especially on the concave side of the asymmetry. Notably, the central region of large N_1 is now caused primarily by shear at the interface between the two dominant flow branches, which although a fundamentally different flow type from the previously symmetric extensional flow, is also capable of stretching polymer molecules, thus generating large normal stresses. On that note, one of the few differences between Figs. 2 and 3 is the increase/decrease in size of the N_1 iso-surface, respectively, likely due to the stress unbounded nature of the UCM model in extensional flows *vs.* the bounded extensional viscosity and shear-thinning behaviour for the sPTT fluid.

The qualitative picture described above is consistent throughout the simulated parameter space, so further plots as given in Figs. 2 and 3 for different ARn would be redundant. Understanding the bifurcation mechanism thus requires the computation of characteristic parameters such as those given in Ref. [8]. Critically, a quantitative measure of flow asymmetry is needed. However, the absence of a scalar streamfunction in 3D flows invalidates the straightforward computation of the asymmetry parameter DQ proposed in Ref. [8]. Considering the vertical symmetry about the XY middle-plane, observed for all simulations in this work, and taking advantage of the eigenvector/eigenvalue calculations described in Section 2, a suitable asymmetry parameter is the cosine of the angle between the two non-vertical eigenvectors of $\nabla\mathbf{u}^\dagger$ at the central stagnation point, $\cos(\theta) = \hat{\mathbf{v}}_1 \cdot \hat{\mathbf{v}}_2$. For symmetric flow, these correspond to the Cartesian unit vectors $(\hat{\mathrm{i}}, \hat{\mathrm{j}})$ and $\cos(\theta) = 0$. Stability diagrams are provided in Figs. 4 and 5, for the UCM and sPTT models, respectively. The sequence of flow states, types of transitions and corresponding De_{crit} strongly depends on the aspect ratio of the cross-slot. Roughly, for both models, at $ARn > 0.5$, two types of flow transition are present: steady bifurcation and, at higher De, onset of time-dependent flow. However, for $ARn < 0.5$, approximately, there is a single, direct transition from steady symmetric flow to unsteady flow. This is an interesting cut-off, since it separates geometries in two broad categories: *deep* channels, $H > D$ and *shallow* channels, $H < D$.

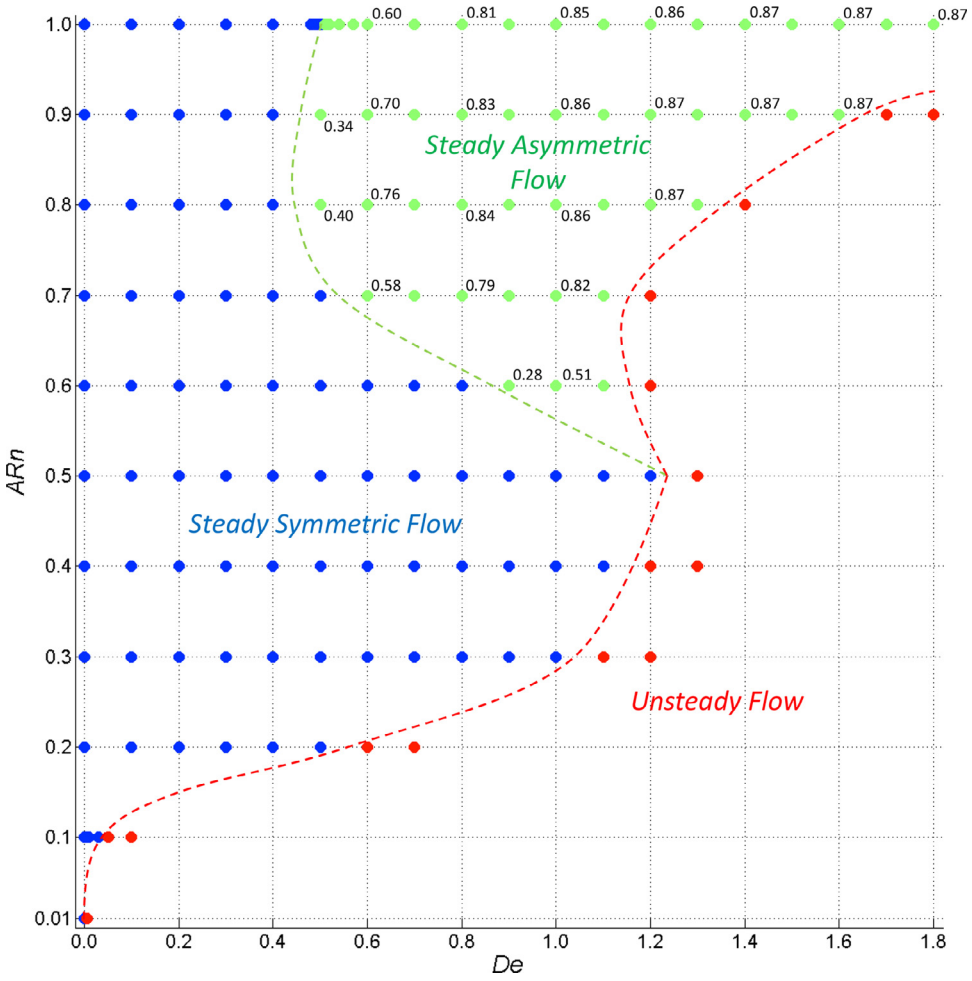

Fig. 5. Stability diagram for sPTT fluid with $\varepsilon = 0.02$ and $\beta = 1/9$. Values are given for the cosine of the angle between non-vertical eigenvectors $(\hat{\mathbf{v}}_1, \hat{\mathbf{v}}_2)$ of $\nabla\mathbf{u}^\dagger$ at the centre of the cross-slot. The dashed lines are a guide to the eye.

Looking specifically at the UCM model, in Fig. 4, for the shallow half of the stability diagram, the single De_{crit} appears to vary approximately linearly with the normalized aspect ratio, suggesting a progressively lower De_{crit} as $AR \to 0$, that is, viscoelastic flow is highly prone to instabilities for very shallow channels, a prediction which may be experimentally tested using *e.g.* a highly elastic Boger fluid [29] in a Hele-Shaw cell [23]. Indeed, in their studies of viscoelastic creeping-flow past a cylinder, McKinley and co-workers [11] used a highly elastic polyisobutylene solution – colloquially known as the MIT Boger fluid and extensively characterized elsewhere [30] – and showed a progressively lower De_{crit} with increased blockage ratio, or in other words, with decreased cylinder-to-wall gap and therefore elevated shear-rate, similar to what is observed for progressively shallower planar cross-slots. This relation between De_{crit} and blockage ratio is further demonstrated in Ref. [19], where it is shown that $1/De_{crit} = \tilde{a} + \tilde{b}/\Lambda$, Λ being the inverse blockage ratio and $\tilde{a}$ and $\tilde{b}$ constants determined by data fitting. For clarity, we underline this comparison between blockage ratio in flow past a cylinder and aspect ratio in a cross-slot is made on the basis of similar shear-rate trends: if $\Lambda \to 1$, the shear-rate increases in the cylinder-to-wall gap; if $AR \to 0$, the shear-rate increases in a cross-slot; in both geometries, the additional shear-rate leads to instability. As for the deep half ($ARn > 0.5$) of the stability map in Fig. 4, the borders separating the symmetric-asymmetric and the asymmetric-unsteady regions appear, although with some variance, to have a constant De_{crit}. Once the channel is sufficiently deep, it seems the UCM fluid behaves as though the channel were infinitely deep. This observed response above a certain AR for UCM-like or more generally Oldroyd-B type fluids may be one of the reasons why three-dimensional effects have generally gone unreported, since microfluidic channels usually are not very shallow (see [31] for examples of five different geometries).

Regarding the stability map for the sPTT fluid (Fig. 5), for the shallow segment of the map ($ARn < 0.5$), again there is a direct transition from steady symmetric to unsteady flow above a critical De, which also decreases concomitantly with the decrease of ARn. As for the deep half ($ARn > 0.5$) of the stability map in Fig. 5, De_{crit} for the symmetric-asymmetric transition is approximately constant for $ARn \geq 0.7$. For the steady-unsteady flow transition a different scenario is observed. Although the stability map in Fig. 5 ranges from $De = 0$ up to $De = 1.8$, further simulations for the two-dimensional, $ARn = 1.0$ case show the steady-unsteady transition occurs at $De_{crit} = 3.75 \pm 0.05$. Since this transition occurs at $De_{crit} = 1.65 \pm 0.05$ for

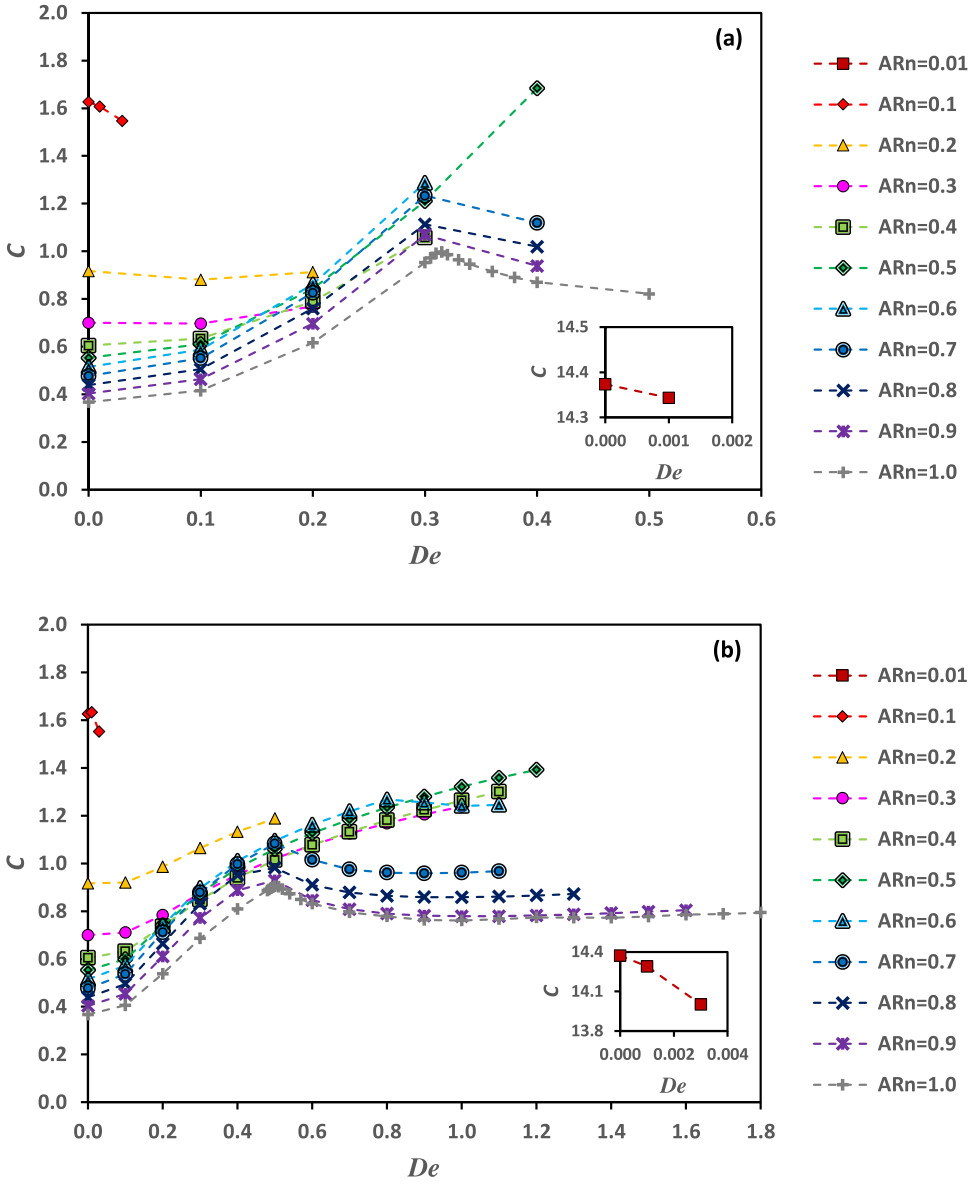

Fig. 6. Extra pressure drop, as indicated by the Couette correction C, for the steady state flow of (a) UCM fluid and (b) sPTT fluid with $\varepsilon = 0.02$ and $\beta = 1/9$.

$ARn = 0.9$, it appears the stability boundary continues to evolve, even for already fairly deep channels. In contrast, the UCM flow exhibits an approximately constant De_{crit} starting at $ARn = 0.5$. Since the parameters of the sPTT model were set at $\varepsilon = 0.02$ and $\beta = 1/9$, ergo the extensibility is large but not infinite and the solvent contribution to viscosity is small but not zero, we conclude that the depth at which a cross-slot channel may be considered a good approximation to a 2D geometry is strongly dependent on the rheological properties of the test fluid.

3.2. Bifurcation lowers resistance to flow

In previous publications concerning the viscoelastic cross-slot bifurcation, the observation that asymmetric flow states are accompanied by a reduction of energy dissipation is often mentioned as a justification for the phenomenon [6,7,32]. If this is the case, a reduction in energy dissipation upon bifurcation should occur regardless of aspect ratio. Data for the extra pressure drop is given in Fig. 6. The extra energy dissipation due to the central slot, relative to the dissipation occurring in the arms is expressed *via* the Couette correction C,

$$C = \frac{\Delta p - \Delta p_{fd}}{2\tau_{w,fd}}, \tag{6}$$

where the subscript fd refers to fully-developed flow, meaning Δp_{fd} would be the pressure drop if the cross-slot had no central slot, *i.e.* considering just fully-developed flow in the inlet and outlet arms. The average corresponding wall shear stress $\tau_{w,fd}$ may be expressed as,

$$2\tau_{w,fd} = D\left|\frac{\Delta p}{L}\right|_{fd} ARn, \tag{7}$$

where $|\Delta p/L|_{fd}$ denotes the constant pressure gradient in the inlet and outlet arms, which are geometrically identical, implying $|\mathrm{d}p/\mathrm{d}x|_{fd} = |\mathrm{d}p/\mathrm{d}y|_{fd} = |\Delta p/L|_{fd}$; L is the distance over which Δp is calculated. Inspection of Fig. 6 shows a decrease in excess pressure drop upon bifurcation for all aspect ratios where the symmetric-asymmetric transition occurs, in agreement with previous literature.

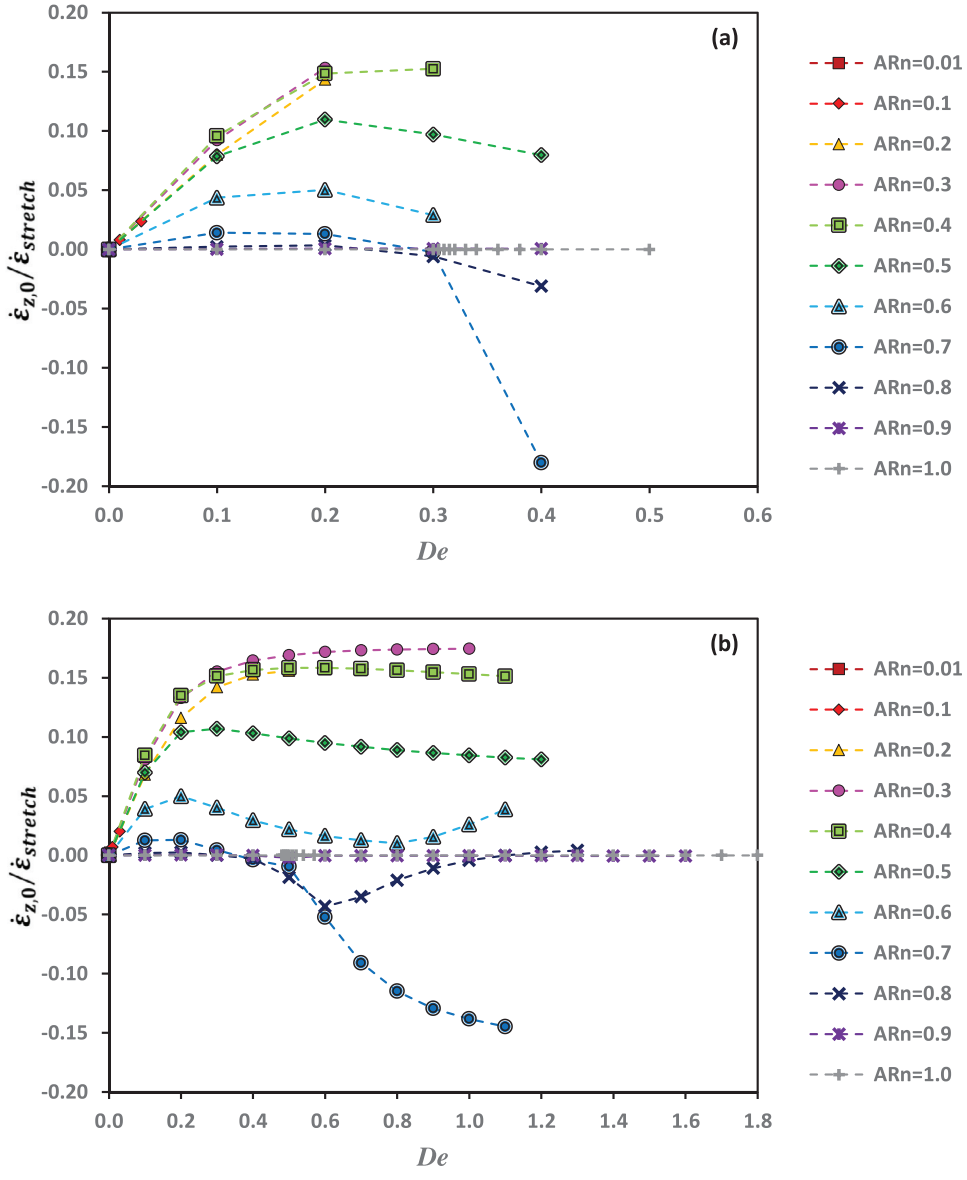

Fig. 7. Strain-rate along the z-direction at the central stagnation point, normalized by the stretch on the central XY plane, for the steady state flow of (a) the UCM fluid and (b) the sPTT fluid, with $\varepsilon = 0.02$ and $\beta = 1/9$. Positive values indicate local stretching and negative values represent local compression.

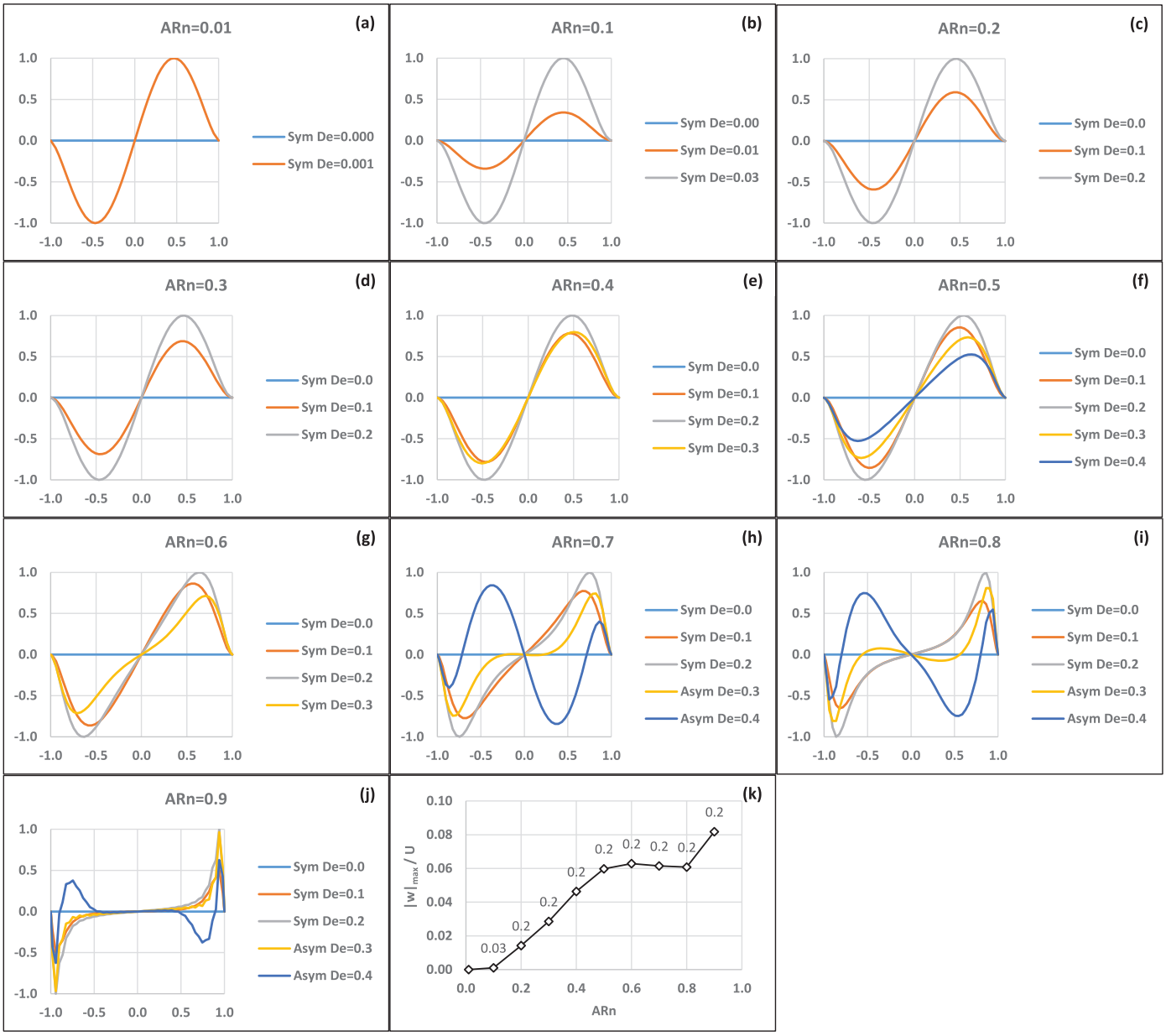

Fig. 8. Velocity profiles along the vertical z-axis for the steady state flow of the UCM fluid. Newtonian flows are also shown at $De = 0.0$. Panels (a–j): vertical axes represent the normalized velocity component $w_n = w/|w|_{max}$, and horizontal axes are the normalized position component $z_n = z/(H/2)$. Values of $|w|_{max}/U$ for each aspect ratio are given in panel (k), with data point labels referring to the corresponding De; at $ARn = 0.01$, the missing De label is 0.001.

3.3. Mechanism of bifurcation in 3D cross-slots

The illustrative results in Figs. 2 and 3 show the emergence of peripheral stagnation points along the z-axis upon bifurcation, which direct matter towards the central stagnation point along the vertical z-direction. By continuity, this implies some of the matter headed towards the centre along the x-direction changes trajectory, with streamlines buckling around it. A more consistent way to characterize this 3D effect is to look at the strain-rate along the z-axis at the centre. At the centre, one of the eigenvectors of $\nabla\mathbf{u}^{\dagger}$ is always parallel to the z-axis, for all simulated cases, and the other two are normal to the z-axis. The corresponding eigenvalue $\dot{\varepsilon}_{z,0}$ is given in Fig. 7, normalized by $\dot{\varepsilon}_{stretch}$ to provide an indication of the relative weight of this vertical component. Furthermore, to illustrate the flow of matter along the central z-axis, velocity profiles of the z-component of velocity are given in Figs. 8 and 9 for UCM and sPTT models, respectively, with stagnation points identifiable by a change in the sign of this velocity component. In general, $\dot{\varepsilon}_{z,0} \to 0$ for the Newtonian limit or the two-dimensional limit. For finite channel depth and fluid elasticity, flows initially have a single stagnation point and $\dot{\varepsilon}_{z,0} \geq 0$. As De increases, the flow field may undergo a steady bifurcation, and at approximately the same De, $\dot{\varepsilon}_{z,0}$ becomes negative and peripheral stagnation points emerge. Furthermore, these peripheral stagnation points move closer to the top/bottom walls for progressively higher De, eventually leading to the formation of two additional stagnation points, to a total of five, as illustrated in Fig. 8(j) for $De = 0.4$ and Fig. 9(i) for $De = 1.3$. Hypothetically, for very deep channels ($ARn > 0.9$), it is possible that more stagnation points form, eventually merging in a *stagnation axis*, seen at the 2D limit. The second pair of peripheral stagnation points also triggers a change in the sign of $\dot{\varepsilon}_{z,0}$ in an already bifurcated flow, *e.g.* $De = 1.3$ at $ARn = 0.8$ in Fig. 7(b). Additionally, although usually the steady bifurcation and the emergence of peripheral stagnation points occur at the same De, in some instances there is a delay between phenomena. For instance, peripheral

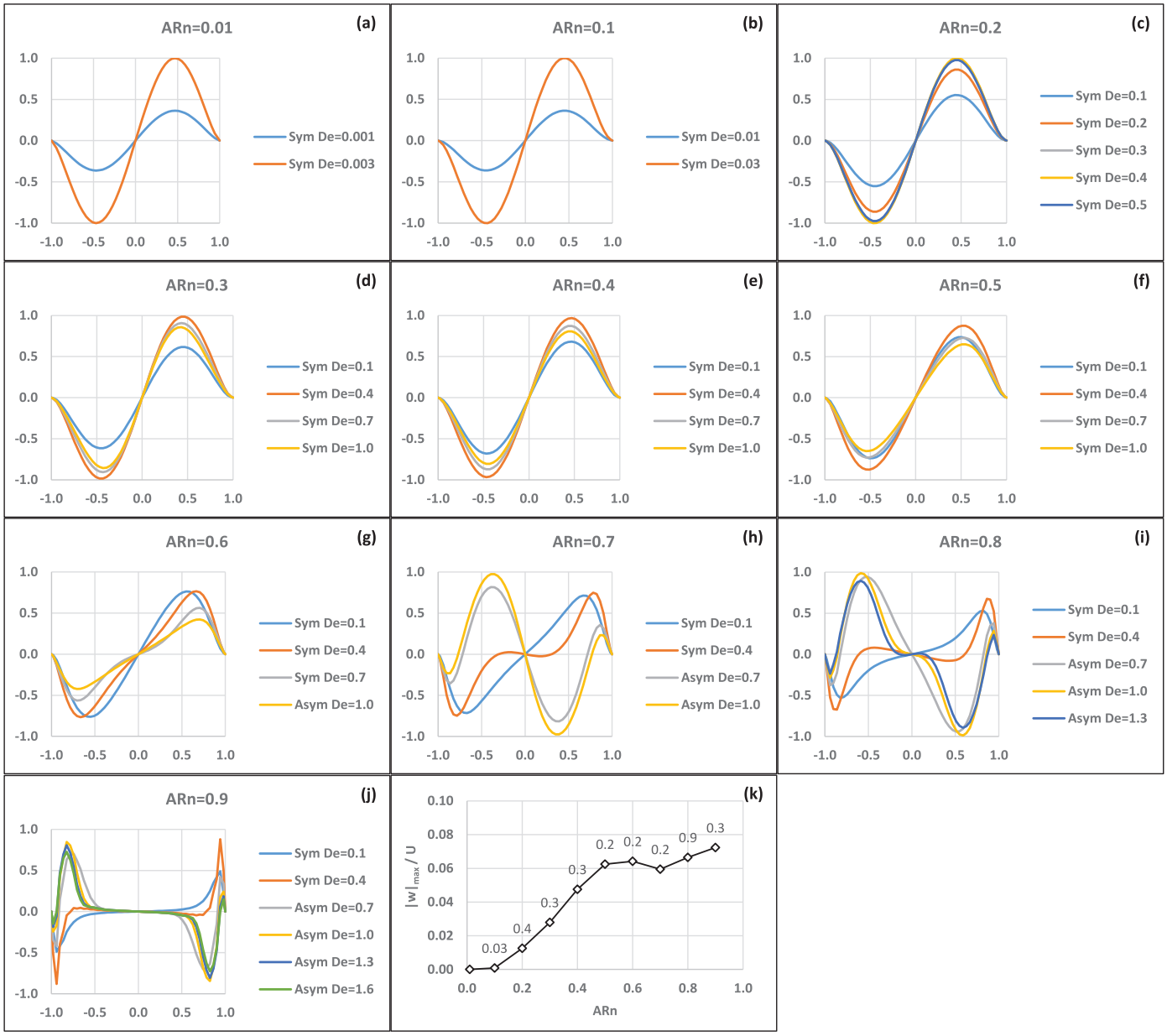

Fig. 9. Velocity profiles along the vertical z-axis for the steady state flow of the sPTT fluid with $\varepsilon = 0.02$ and $\beta = 1/9$. For better visibility, only some De are shown. Panels (a–j): vertical axes represent the normalized velocity component $w_n = w/|w|_{max}$, and horizontal axes are the normalized position component $z_n = z/(H/2)$. Values of $|w|_{max}/U$ for each aspect ratio are given in panel (k), with data point labels referring to the corresponding De; at $ARn = 0.01$, the missing De label is 0.003.

stagnation points start appearing prior to bifurcation for $De = 0.4$ in Fig. 9(h)–(j), and bifurcation is seen to occur without the immediate formation of peripheral stagnation points for $De = 0.3$ in Fig. 8(j) and $De = 1.0$ in Fig. 9(g). That such delays show no bias towards either phenomenon makes it difficult to establish a relation of cause and effect. Work on viscoelastic creeping-flow around cylinders [11–13] has revealed the formation of steady-state, three-dimensional wake cellular structures above a critical Deborah number, shown in [11] to be a function of the cylinder blockage ratio. Furthermore, streamlines in the wake form bundles along the neutral axis of the cylinder (*cf.* Fig. 26 in [11] and Fig. 4 in [13]). Thus, the fluid selects a set of paths along which local, relative velocities become higher, as shown by the convergence of streamlines. Considering the steady bifurcation in planar cross-slots is accompanied by a reduction in dissipated energy, as shown by the reduced extra pressure drop (Fig. 6), the asymmetric flow field necessarily favours paths of least resistance, in a manner akin to the wake cells observed for creeping-flow around cylinders. We hypothesize that the emergence of vertical flow upon steady bifurcation relates to the global decrease in energy dissipation. Furthermore, as shown in Fig. 10, gaps of low streamwise tensile stress $\tau_{ss} = \mathbf{u}^{\dagger}\boldsymbol{\tau}\mathbf{u}/\|\mathbf{u}\|^2$, computed as a projection of the stress tensor $\boldsymbol{\tau}$ onto the local velocity field streamline direction, $\mathbf{u}/\|\mathbf{u}\|$, are present along the central z-axis. Here $\|\mathbf{u}\|$ is the local velocity magnitude given by $\|\mathbf{u}\| = \sqrt{u^2 + v^2 + w^2}$. Since τ_{ss} may be construed as an indicator of resistance to flow, we speculate that the emergent vertical flow upon bifurcation contributes, locally, to the observed global reduction in extra pressure drop.

3.4. Local evaluation of the Pakdel–McKinley criterion

The strong flow curvature near the four cross-slot corners is potentially responsible for the second transition, to an unsteady flow pattern, and we therefore apply the ideas developed by McKinley and co-workers to investigate this possibility. The Pakdel–McKinley

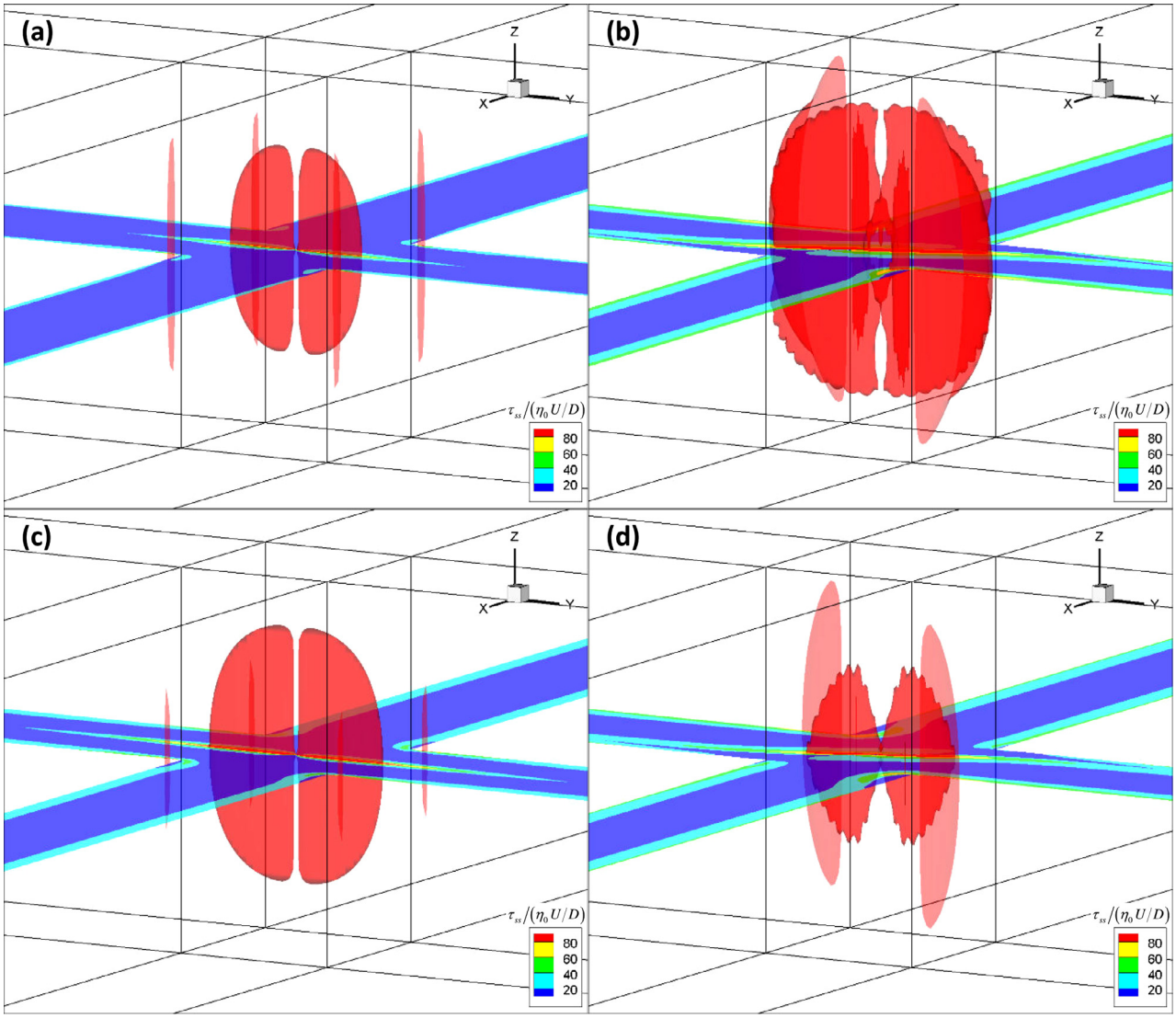

Fig. 10. Iso-surfaces and *XY* centre plane of the normalized streamwise stress $\tau_{ss}/(\eta_0 U/D)$, for $ARn = 0.7$. (a) Symmetric UCM flow at $De = 0.2$. (b) Asymmetric UCM flow at $De = 0.4$. (c) Symmetric sPTT flow at $De = 0.5$. (d) Asymmetric sPTT flow at $De = 1.1$. Iso-surfaces are drawn at $\tau_{ss}/(\eta_0 U/D) = 80$. sPTT fluid with $\varepsilon = 0.02$ and $\beta = 1/9$.

criterion can be written as [19],

$$M = \sqrt{\frac{\lambda_0 U}{R}\frac{\tau_{ss}}{\eta_0 \dot{\gamma}}}, \tag{8}$$

where $\lambda_0 U = l$ is the characteristic length over which perturbations to the base stress and velocity fields relax, R is the streamline radius of curvature, τ_{ss} is the streamwise tensile stress, η_0 is the zero-shear-rate shear viscosity and $\dot{\gamma}$ is the local deformation rate. Conversion of this definition of the criterion to a form amenable to local evaluation in three-dimensional flows requires the substitution of characteristic values by local values. Considering the first non-dimensional group $\lambda_0 U/R$, λ_0 is substituted by its effective counterpart – which in this work is evaluated as $\lambda_{eff} = \lambda_0/g(\boldsymbol{\tau})$ – given that depending on flow conditions and fluid rheology, the local relaxation time may vary. Likewise the characteristic streamwise velocity U is substituted by the local velocity magnitude and the radius of curvature R is substituted by the local streamline radius of curvature r, yielding, *via* the parametric definition, $r = \|\mathbf{u}\|^3/\|\mathbf{u}\times\dot{\mathbf{u}}\|$. Here we note $\dot{\mathbf{u}}$ is the material derivative of the velocity vector, which reduces to $\mathbf{u}\cdot\nabla\mathbf{u}$ for steady-state flow. Regarding the second dimensionless group $\tau_{ss}/(\eta_0\dot{\gamma})$, τ_{ss} is the streamwise tensile stress, as defined in the previous section. Concerning the shear viscosity, flow conditions and fluid rheology may result in local variations in viscosity, such that the effective shear viscosity η_{eff} is better suited for local evaluation. For the purposes of this study, η_{eff} is the shear viscosity evaluated at local conditions, $\eta_{eff} = \eta_s + \eta_{p,0}/g(\boldsymbol{\tau})$ for the sPTT fluid. Lastly, the local deformation rate may be expressed as the magnitude of the strain-rate tensor, $\dot{\gamma} = \|\dot{\boldsymbol{\gamma}}\| = \sqrt{1/2\dot{\boldsymbol{\gamma}} : \dot{\boldsymbol{\gamma}}^{\dagger}}$.

A further issue when considering the local evaluation of M is the rotational nature of flow in certain regions not too far from the corners of the cross-slot. In these locations, the magnitude of the strain-rate tensor approaches zero, leading to high values of M. However, the lack of shear in solid-like rotational flows invalidates the micromechanical model of purely elastic instabilities proposed by Larson et al. [33]. Thus, large values of M in rotational flow regions do not necessarily imply proneness to instability. The problem may be remedied by substitution of the term $\eta_{eff}\|\dot{\boldsymbol{\gamma}}\|$ by the magnitude of the stress tensor $\|\boldsymbol{\tau}\|_F$. Here we use the Frobenius norm ($\|\cdot\|_F$), so that the resulting dimensionless group $\tau_{ss}/\|\boldsymbol{\tau}\|_F$ will vary between zero, when normal stresses are weak, and one, when the tensile normal stress τ_{ss}

dominates, as happens in highly elastic shear or extensional flows. Therefore in strongly extensional flows, M^* is approximately given by $\sqrt{\lambda_{eff}\|\mathbf{u}\|/r}$, such as in the optimized shape cross-slot extensional rheometer [34], where extensional flow is attained for finite values of r and therefore the criterion has a non-trivial value. To avoid confusion, we use here the notation M^* to represent the modified Pakdel–McKinley criterion,

$$M^* = \sqrt{\frac{\lambda_{eff}\|\mathbf{u}\|}{r}\frac{\tau_{ss}}{\|\boldsymbol{\tau}\|_F}}. \quad (9)$$

With the standard Pakdel–McKinley criterion the instability due to the coupling of tensile stresses along curved streamlines and the base shear-flow sets in when M is larger than a critical value, which depends on the flow geometry. Here, since M^* is locally evaluated, the critical condition defining a flow transition is given by the maximum of the M^* scalar field over the flow domain. Hence, for each constitutive model-geometry pair, the maximum value of M^* at the highest De immediately prior to each flow transition was assessed and is given in Table 2. Critical values of the modified Pakdel–McKinley criterion are consistent with available literature, in which the characteristic range of M is approximately $1-10$ for various model geometries [18–20,35–37]. The steady bifurcation occurs at consistently lower M^*_{crit} than the onset of time-dependent flow, regardless of whether the flow field is in a symmetric or asymmetric configuration prior to the latter transition. Furthermore, values of M^*_{crit} pertaining specifically to the UCM fluid are somewhat insensitive to the aspect ratio of the channel. The small variability of M^*_{crit} indicates the usefulness of this modified criterion in the prediction of critical flow transitions. Fig. 11 shows the progression of the highest value of M^* for each geometry and constitutive model. For the UCM model, the values of M^*_{max} increase monotonically, up to the transition to time-dependent flow, seemingly ignoring the steady flow bifurcation. A similar scenario is observed for the sPTT model in Fig. 11(b), although a momentary decrease in M^*_{max} occurs between $De = 0.6$ and $De = 0.8$, regardless of aspect ratio – so long as the flow is still steady – or whether the flow field is in a symmetric or asymmetric configuration.

Local evaluation of M^* allows the construction of scalar stability maps, illustrated in Figs. 12 and 13, thus facilitating the location of instability-driving regions within the flow field. The highest value of M^* is always located at the centre plane ($z = 0$), approximately along the diagonals of the slot, closer to the corners than to the stagnation point, but not adjacent to the former. Furthermore, concerning

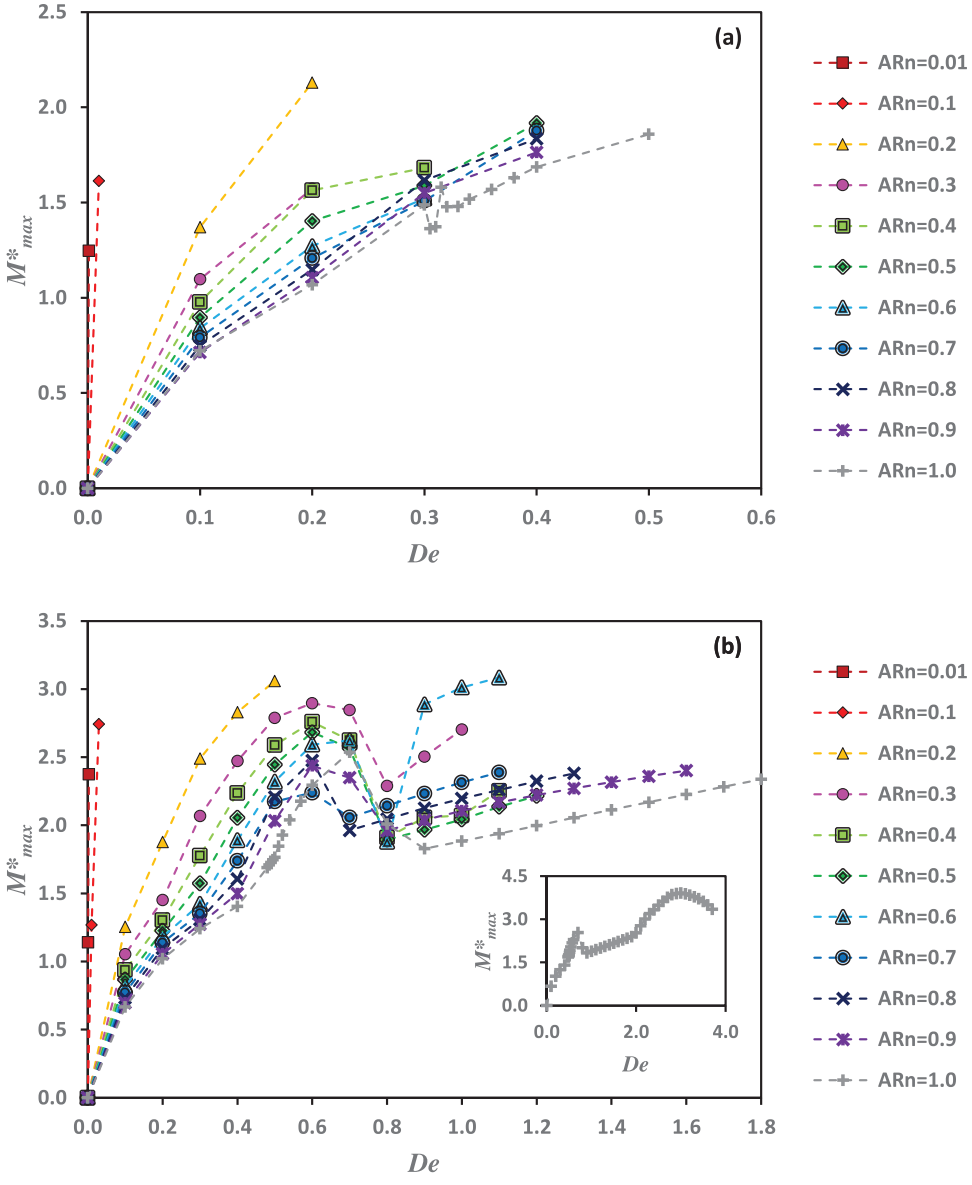

Fig. 11. Maximum value of the modified Pakdel–McKinley criterion M^*_{max}, for the (a) UCM and (b) sPTT models, the latter with $\varepsilon = 0.02$ and $\beta = 1/9$.

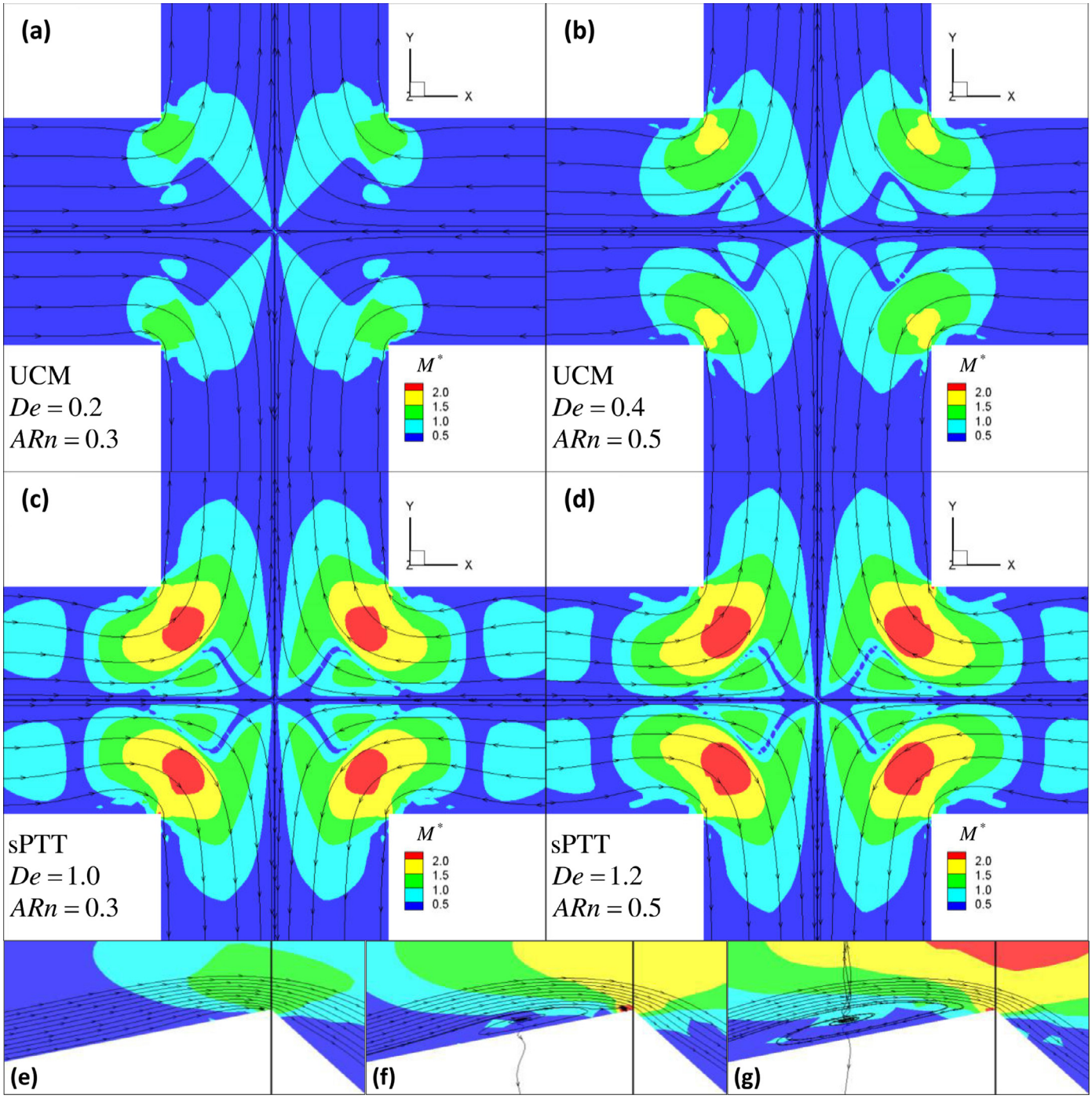

Fig. 12. Illustrative contour plots of the modified Pakdel–McKinley criterion M^* with superimposed streamlines, for the transition from steady symmetric to unsteady flow. Plots are given for the *XY* centre plane, at $z = 0$, for the highest simulated *De* prior to each transition. The constitutive model, Deborah number and normalized aspect ratio are indicated in each of the four main panels. Panels (e), (f) and (g): slanted, 6× zoomed-in view of the southwest corner of the *XY* centre plane. Panel (g) corresponds to main panel (c), while (e) and (f) are given for $De = 0.2$ and $De = 0.6$, for the same fluid and geometry.

the dip in the value of M^*_{max} between $De = 0.6$ and $De = 0.8$, shown in Fig. 11(b), we can see from Fig. 12(e)–(g) the formation of three-dimensional structures analogous to 2D lip vortices. These structures cause an increase in the radius of curvature of the flow in the regions where M^* is highest, lowering its maximum value, and are also responsible for shifting matter vertically near the corners. However, since their emergence is consistently at approximately $De = 0.6$ they do not appear to directly influence the critical flow transitions studied elsewhere in this work. In Fig. 13, the M^* field is shown at the same height as emerging peripheral stagnation points. Upon steady bifurcation, in the $z = 0$ plane, the relative size of high M^* regions is enhanced on the concave side of the asymmetry and suppressed on the convex side. Maximum values of M^* near convex side corners are shifted vertically, and appear in the same planes as peripheral stagnation points - compare northwest or southeast cross-slot corners in Fig. 13(b), (c) and (e), (f). Thus it seems that a secondary effect of bifurcation is the spreading of instability prone regions along the *z*-direction.

Table 2
Critical values of the modified, locally evaluated Pakdel–McKinley criterion M^*_{crit} for all observed flow transitions. *Types of transitions:* Sym–Unst, transition from a steady symmetric state to a time-dependent flow; Sym–Asym, flow remains steady, but bifurcates from a symmetric to an asymmetric configuration; Asym–Unst, transition from a steady asymmetric state to unsteady flow. Values are given for the last stable simulation prior to transition. STD: standard-deviation.

Model	Transition	*ARn*	De_{crit}	M^*_{crit}	$\overline{M^*_{crit}} \pm$ STD
UCM	Sym–Unst	0.01	0.001	1.2	1.7 ± 0.3
		0.1	0.03	2.2	
		0.2	0.2	2.1	
		0.3	0.2	1.6	
		0.4	0.3	1.7	
		0.5	0.4	1.9	
		0.6	0.3	1.5	
	Sym–Asym	0.7	0.2	1.2	1.2 ± 0.2
		0.8	0.2	1.1	
		0.9	0.2	1.1	
		1.0	0.3	1.5	
	Asym–Unst	0.7	0.4	1.9	1.8 ± 0.1
		0.8	0.4	1.8	
		0.9	0.4	1.8	
		1.0	0.5	1.9	
sPTT $\beta = 1/9$ $\varepsilon = 0.02$	Sym–Unst	0.01	0.003	2.4	2.6 ± 0.3
		0.1	0.3	2.7	
		0.2	0.5	3.1	
		0.3	1.0	2.7	
		0.4	1.1	2.3	
		0.5	1.2	2.2	
	Sym–Asym	0.6	0.8	1.9	1.8 ± 0.3
		0.7	0.5	2.2	
		0.8	0.4	1.6	
		0.9	0.4	1.5	
		1.0	0.5	1.8	
	Asym–Unst	0.6	1.1	3.1	2.7 ± 0.5
		0.7	1.1	2.4	
		0.8	1.3	2.4	
		0.9	1.6	2.4	
		1.0	3.7	3.4	

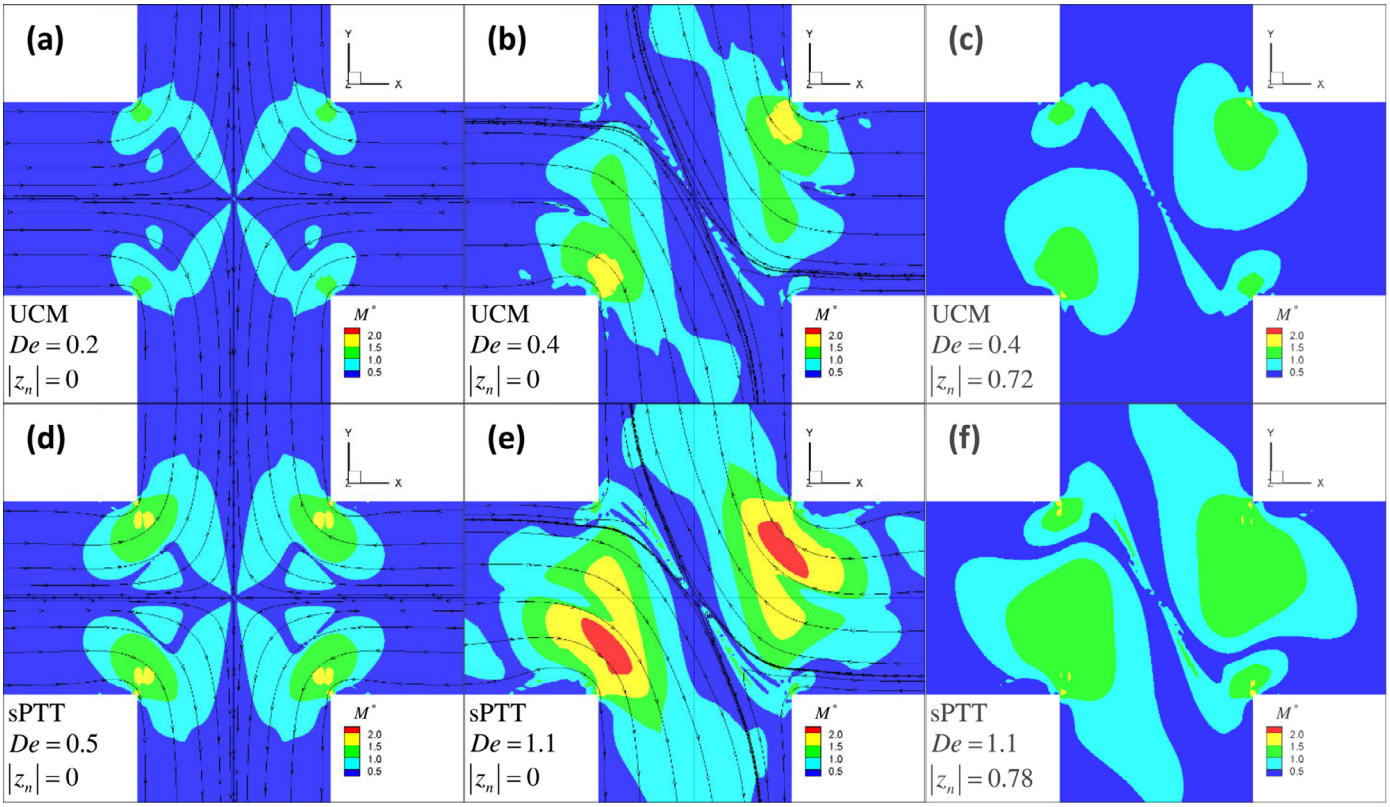

Fig. 13. Contour maps of the modified Pakdel–McKinley criterion M^* for $ARn = 0.7$, at the highest simulated *De* prior to each flow transition. The constitutive model, Deborah number and normalized height coordinate of each horizontal map, defined as $z_n = z/(H/2)$, are given in each panel. Maps are shown (a, d) prior to the steady bifurcation and (b, e)–(c, f) prior to the onset of time-dependent flow. Maps drawn in (c, f) are centred at the location of a peripheral stagnation point; no streamlines are represented due to the three-dimensional nature of flow in these planes.

4. Conclusions

Based on the evidence presented in this work, we propose the mechanism of three-dimensional planar cross-slot steady flow bifurcations is characterized by a buckling-type instability, by which flow is redirected *via* paths of least resistance, therefore reducing energy dissipation. Since the path of highest resistance is given by a direct approach to the central stagnation point along the inlet axis, streamlines tend to curve around it along the *XY* plane when normal compressive stresses increase concomitantly with *De*, as a consequence of progressively larger elasticity. Consequently, the central stagnation point receives matter *via* newly formed, paired and symmetrically-located peripheral stagnation points along the central vertical axis. Additionally, based on the sequence of flow transitions, creeping-flow of viscoelastic fluids in cross-slots may be divided in two regimes: the shallow-channel regime for $ARn < 0.5$ and the deep-channel regime for $ARn > 0.5$. In the shallow-channel regime, flow transitions directly from a steady symmetric pattern to a time-dependent flow. On the other hand, in the deep-channel regime, which ultimately encompasses the limiting two-dimensional case, the flow first bifurcates from a steady symmetric to a steady asymmetric configuration, and at higher *De* transitions to unsteady flow. Therefore, square-section channels, being at the intersection of the two regimes, may exhibit an unclear sequence of transitions. Furthermore, an assessment of flow stability *via* the local computation of a modified Pakdel–McKinley criterion indicates the presence of potentially unstable flow regions approximately along the diagonals of the central *XY* plane. Peripheral stagnation points generated by steady bifurcation may further contribute to the destabilization of flow, as shown by the presence of secondary instability prone regions in the corresponding *z*-planes.

Acknowledgements

A.M. Afonso thanks Fundação para a Ciência e a Tecnologia (FCT), Portugal, for financial support through scholarship SFRH/BPD/75436/2010. F.A. Cruz and M.A. Alves acknowledge funding from the European Research Council (ERC), under the European Commission "Ideas" specific programme of the 7th Framework Programme (Grant agreement no. 307499).

References

[1] R.G. Larson, Instabilities in viscoelastic flows, Rheol. Acta 31 (1992) 213–263, doi:10.1007/BF00366504.
[2] E.S.G. Shaqfeh, Purely elastic instabilities in viscometric flows, Annu. Rev. Fluid Mech. 28 (1996) 129–185, doi:10.1146/annurev.fl.28.010196.001021.
[3] A. Groisman, V. Steinberg, Elastic turbulence in a polymer solution flow, Nature 405 (2000) 53–55, doi:10.1038/35011019.
[4] A. Groisman, V. Steinberg, Efficient mixing at low Reynolds numbers using polymer additives, Nature 410 (2001) 905–908, doi:10.1038/35073524.
[5] P.E. Arratia, C.C. Thomas, J. Diorio, J.P. Gollub, Elastic instabilities of polymer solutions in cross-channel flow, Phys. Rev. Lett. 96 (2006) 144502, doi:10.1103/PhysRevLett.96.144502.
[6] R.J. Poole, M.A. Alves, P.J. Oliveira, Purely elastic flow asymmetries, Phys. Rev. Lett. 99 (2007) 164503, doi:10.1103/PhysRevLett.99.164503.
[7] G.N. Rocha, R.J. Poole, M.A. Alves, P.J. Oliveira, On extensibility effects in the cross-slot flow bifurcation, J. Non-Newt. Fluid Mech. 156 (2009) 58–69, doi:10.1016/j.jnnfm.2008.06.008.
[8] F.A. Cruz, R.J. Poole, A.M. Afonso, F.T. Pinho, P.J. Oliveira, M.A. Alves, A new viscoelastic benchmark flow: stationary bifurcation in a cross-slot, J. Non-Newt. Fluid Mech. 214 (2014) 57–68, doi:10.1016/j.jnnfm.2014.09.015.
[9] L. Xi, M.D. Graham, A mechanism for oscillatory instability in viscoelastic cross-slot flow, J. Fluid Mech. 622 (2009) 145, doi:10.1017/S0022112008005119.
[10] A.M. Afonso, M.A. Alves, F.T. Pinho, Purely elastic instabilities in three-dimensional cross-slot geometries, J. Non-Newt. Fluid Mech. 165 (2010) 743–751, doi:10.1016/j.jnnfm.2010.03.010.
[11] G.H. McKinley, R.C. Armstrong, R.A. Brown, The wake instability in viscoelastic flow past confined circular cylinders, Philos. Trans. R. Soc. London. Ser. A: Phys. Eng. Sci. 344 (1993) 265–304, doi:10.1098/rsta.1993.0091.
[12] A.H. Shiang, A. Öztekin, J.-C. Lin, D. Rockwell, Hydroelastic instabilities in viscoelastic flow past a cylinder confined in a channel, Exp. Fluids 28 (2000) 128–142, doi:10.1007/s003480050017.
[13] M. Sahin, Parallel large-scale numerical simulations of purely-elastic instabilities behind a confined circular cylinder in a rectangular channel, J. Non-Newt. Fluid Mech. 195 (2013) 46–56, doi:10.1016/j.jnnfm.2012.11.011.
[14] M.S.N. Oliveira, F.T. Pinho, R.J. Poole, P.J. Oliveira, M.A. Alves, Purely elastic flow asymmetries in flow-focusing devices, J. Non-Newt. Fluid Mech. 160 (2009) 31–39, doi:10.1016/j.jnnfm.2009.02.010.
[15] J. Soulages, M.S.N. Oliveira, P.C. Sousa, M.A. Alves, G.H. McKinley, Investigating the stability of viscoelastic stagnation flows in T-shaped microchannels, J. Non-Newt. Fluid Mech. 163 (2009) 9–24, doi:10.1016/j.jnnfm.2009.06.002.
[16] A.M. Afonso, M.A. Alves, R.J. Poole, P.J. Oliveira, F.T. Pinho, Viscoelastic flows in mixing-separating cells, J. Eng. Math. 71 (2011) 3–13, doi:10.1007/s10665-010-9384-x.
[17] R.J. Poole, M.A. Alves, A.M. Afonso, F.T. Pinho, P.J. Oliveira, Purely-elastic flow instabilities in a microfluidic cross-slot geometry, in: Proceedings of the AIChE 2007 Annual Meeting, 2007.
[18] P. Pakdel, G. McKinley, Elastic instability and curved streamlines, Phys. Rev. Lett. 77 (1996) 2459–2462, doi:10.1103/PhysRevLett.77.2459.
[19] G.H. McKinley, P. Pakdel, A. Öztekin, Rheological and geometric scaling of purely elastic flow instabilities, J. Non-Newt. Fluid Mech. 67 (1996) 19–47, doi:10.1016/S0377-0257(96)01453-X.
[20] A.M. Afonso, F.T. Pinho, M.A. Alves, Electro-osmosis of viscoelastic fluids and prediction of electro-elastic flow instabilities in a cross slot using a finite-volume method, J. Non-Newt. Fluid Mech. 179-180 (2012) 55–68, doi:10.1016/j.jnnfm.2012.05.004.
[21] J.G. Oldroyd, On the formulation of rheological equations of state, Proc. R. Soc. A: Math. Phys. Eng. Sci. 200 (1950) 523–541, doi:10.1098/rspa.1950.0035.
[22] N. Phan-Thien, R.I. Tanner, A new constitutive equation derived from network theory, J. Non-Newt. Fluid Mech. 2 (1977) 353–365, doi:10.1016/0377-0257(77)80021-9.
[23] H.S. Hele-Shaw, The flow of water, Nature 58 (1898) 34–36, doi:10.1038/058034a0.
[24] N. Phan-Thien, A nonlinear network viscoelastic model, J. Rheol. 22 (1978) 259, doi:10.1122/1.549481.
[25] P.J. Oliveira, F.T. Pinho, G.A. Pinto, Numerical simulation of non-linear elastic flows with a general collocated finite-volume method, J. Non-Newt. Fluid Mech. 79 (1998) 1–43, doi:10.1016/S0377-0257(98)00082-2.
[26] M.A. Alves, P.J. Oliveira, F.T. Pinho, A convergent and universally bounded interpolation scheme for the treatment of advection, Int. J. Numer. Meth. Fluids 41 (2003) 47–75, doi:10.1002/fld.428.
[27] A.M. Afonso, P.J. Oliveira, F.T. Pinho, M.A. Alves, The log-conformation tensor approach in the finite-volume method framework, J. Non-Newt. Fluid Mech. 157 (2009) 55–65, doi:10.1016/j.jnnfm.2008.09.007.
[28] R. Fattal, R. Kupferman, Constitutive laws for the matrix-logarithm of the conformation tensor, J. Non-Newt. Fluid Mech. 123 (2004) 281–285, doi:10.1016/j.jnnfm.2004.08.008.
[29] D.V. Boger, A highly elastic constant-viscosity fluid, J. Non-Newt. Fluid Mech. 3 (1977) 87–91, doi:10.1016/0377-0257(77)80014-1.
[30] L.M. Quinzani, G.H. McKinley, R.A. Brown, R.C. Armstrong, Modeling the rheology of polyisobutylene solutions, J. Rheol. 34 (1990) 705, doi:10.1122/1.550148.
[31] F.J. Galindo-Rosales, L. Campo-Deaño, P.C. Sousa, V.M. Ribeiro, M.S.N. Oliveira, M.A. Alves, F.T. Pinho, Viscoelastic instabilities in micro-scale flows, Exp. Therm. Fluid Sci. 59 (2014) 128–139, doi:10.1016/j.expthermflusci.2014.03.004.
[32] H.J. Wilson, Open mathematical problems regarding non-Newtonian fluids, Nonlinearity 25 (2012) R45–R51, doi:10.1088/0951-7715/25/3/R45.
[33] R.G. Larson, E.S.G. Shaqfeh, S.J. Muller, A purely elastic instability in Taylor–Couette flow, J. Fluid Mech. 218 (1990) 573–600, doi:10.1017/S0022112090001124.
[34] S.J. Haward, M.S.N. Oliveira, M.A. Alves, G.H. McKinley, Optimized cross-slot flow geometry for microfluidic extensional rheometry, Phys. Rev. Lett. 109 (2012) 128301, doi:10.1103/PhysRevLett.109.128301.
[35] A. Öztekin, B. Alakus, G.H. McKinley, Stability of planar stagnation flow of a highly viscoelastic fluid, J. Non-Newt. Fluid Mech. 72 (1997) 1–29, doi:10.1016/S0377-0257(97)00021-9.
[36] R.J. Poole, F.T. Pinho, M.A. Alves, P.J. Oliveira, The effect of expansion ratio for creeping expansion flows of UCM fluids, J. Non-Newt. Fluid Mech. 163 (2009) 35–44, doi:10.1016/j.jnnfm.2009.06.004.
[37] J. Zilz, R.J. Poole, M.A. Alves, D. Bartolo, B. Levaché, A. Lindner, Geometric scaling of a purely elastic flow instability in serpentine channels, J. Fluid Mech. 712 (2012) 203–218, doi:10.1017/jfm.2012.411.